In vivo evaluation of ankle kinematics and tibiotalar joint contact strains using digital volume correlation and 3 T clinical MRI

Saman Tavana [a,b,*], Jeffrey N. Clark [a], Choon Chiet Hong [c,d], Nicolas Newell [b], James D. Calder [b,c], Ulrich Hansen [a]

[a] Department of Mechanical Engineering, Imperial College London, London SW7 2AZ, UK
[b] Department of Bioengineering, Imperial College London, London SW7 2AZ, UK
[c] Fortius Clinic, 17 Fitzhardinge St, London W1H 6EQ, UK
[d] Department of Orthopaedic Surgery, National University Hospital of Singapore, Singapore

ARTICLE INFO

ABSTRACT

Background: In vivo evaluation of ankle joint biomechanics is key to investigating the effect of injuries on the mechanics of the joint and evaluating the effectiveness of treatments. The objectives of this study were to 1) investigate the kinematics and contact strains of the ankle joint and 2) to investigate the correlation between the tibiotalar joint contact strains and the prevalence of osteochondral lesions of the talus distribution.
Methods: Eight healthy human ankle joints were subjected to compressive load and 3 T MRIs were obtained before and after applying load. The MR images in combination with digital volume correlation enabled non-invasive measurement of ankle joint kinematics and tibiotalar joint contact strains in three dimensions.
Findings: The total translation of the calcaneus was smaller (0.48 ± 0.15 mm, $p < 0.05$) than the distal tibia (0.93 ± 0.16 mm) and the talus (1.03 ± 0.26 mm). These movements can produce compressive and shear joint contact strains (approaching 9%), which can cause development of lesions on joints. 87.5% of peak tensile, compressive, and shear strains in the tibiotalar joint took place in the medial and lateral zones.
Interpretation: The findings suggested that ankle bones translate independently from each other, and in some cases in opposite directions. These findings help explain the distribution of osteochondral lesions of the talus which have previously been observed to be in medial and lateral regions of the talar dome in 90% of cases. They also provide a reason for the central region of talar dome being less susceptible to developing osteochondral lesions.

1. Introduction

The in vivo assessment of the ankle joint kinematics is crucial to better understand normal and pathological foot motions, to investigate the effect of injuries on the mechanics of the joint, and to evaluate the effectiveness of operative treatments, which aim to restore normal motion to the ankle (Guettler et al., 2004; Hintermann et al., 2002). Lateral ankle ligament sprains are one of the most common sport injuries and can change the kinematics of the ankle joint, causing instability and altering the range of motion (Hirose et al., 2004; Ogilvie-Harris et al., 1997; Rosenbaum et al., 1998; Valderrabano et al., 2006). Previous studies have found a link between changes in the kinematics of the ankle and the development of osteoarthritis (Harrington, 1979; Hintermann et al., 2002; Hirose et al., 2004; Rosenbaum et al., 1997; Taga et al.,

1993; Valderrabano et al., 2006). Additionally, abnormal kinematics caused by lateral ligamentous laxity or rupture can change the load distribution over the joint, leading to the formation of osteochondral lesions of the talus (OLTs) and arthritic changes in the ankle (Guettler et al., 2004; Hirose et al., 2004; O'Loughlin et al., 2010). Therefore, in vivo evaluation of ankle joint kinematics and joint contact strains will add information to current body of knowledge and aid clinical decision-making in terms of treatment plans for patients with ankle injuries. In clinical practice, the ability to accurately investigate ankle kinematics is important, specifically where operational treatment involves total ankle arthroplasty that requires replicating the native joint kinematics. This is important to implant designers who can adapt designs while developing joint replacement devices to mimic the kinematics of the native ankle joint. This will enable them to avoid transmission of abnormal stresses to

---

* Corresponding author at: Room 774, Department of Mechanical Engineering, South Kensington Campus, Imperial College London, London SW7 2AZ, UK.
E-mail address: s.tavana17@imperial.ac.uk (S. Tavana).

the adjacent joints that can cause premature wear and tear. Additionally, the ankle joint contact strains can serve as functional biomechanical markers for healthy, pathologic, and repaired joints and can therefore be used to inform clinical treatment strategies such as repairing lateral ligament injuries to restore physiological ankle joint kinematics to reduce abnormal stresses on the joint leading to OLTs (Hong and Calder, 2022; Wainright et al., 2012). The ankle is a complex structure that experiences complex movements during physiological activities (Dettwyler et al., 2004; Siegler et al., 1988). Because of this anatomical complexity, it is technically difficult to quantify the kinematics of the ankle, and there is a lack of direct, non-invasive measurement techniques for in vivo quantification of joint contact strains.

The kinematics of the tibiotalar and subtalar joints have been previously investigated using both in vitro (Siegler et al., 1988) and in vivo techniques. The most commonly used in vivo technique was the use of external reflective surface skin markers in combination with tracking cameras (Di Marco et al., 2016; Lundberg and Svensson, 1993; Montefiori et al., 2019; Nichols et al., 2017; Scott and Winter, 1991; van den Bogert et al., 1994). Although using skin markers and tracking cameras has the potential to measure dynamic motions during gait, there are some limitations associated with the technique, such as the independent movement of skin markers from the bone, difficulties in identifying the joint centre, inability to provide 3D data, and measurement errors due to the variability in attachment of the markers (Bauman and Chang, 2010; Di Marco et al., 2016; Gorton 3rd et al., 2009). Additionally, due to the lack of external landmarks to attach the markers to the talus, it is not possible to measure motions of the talus and the tibiotalar joint independently. To overcome some of these limitations, previous studies have used markers attached to implanted intracortical bone pins (Arndt et al., 2004; Arndt et al., 2006). However, the invasive nature of this technique renders it impractical for clinical applications. Three-dimensional rigid registration of clinical CT (Beimers et al., 2008) and MRI (Fassbind et al., 2011; Goto et al., 2009; Sheehan, 2010) have also been proposed to address in vivo ankle joint kinematics in non-load-bearing conditions. Rigid registration of MR images can non-invasively quantify 3D kinematics of the ankle with an accuracy ranging from 500 to 600 μm (Goto et al., 2009).

Previous studies combined dual fluoroscopic images with MRI to approximate the tibiotalar contact strain (Bischof et al., 2010; Caputo et al., 2009; Li et al., 2008; Wan et al., 2006, 2008). However, it has been shown that this technique is prone to large errors and variability between observers (Bischof et al., 2010), and might be harmful to patients as it involves high exposure to ionising radiation (Mahesh, 2001). Recently, Peña Fernández et al. (2020) successfully combined image-based digital volume correlation (DVC) analysis with weight-bearing clinical CT to calculate the kinematics of the subtalar joint during inversion and eversion motions, with a precision ranging from 20 to 250 μm. Although this technique uses images acquired in a full weight-bearing configuration, the radiation associated with clinical CT is a limitation that reduces its suitability for widespread use on patients. The invasive nature of the previously developed techniques and their need for using hardware that is not readily available in a hospital setting have hindered the adoption of these techniques in clinical practice. A previous study by our group identified that implementing DVC in combination with 3 T T1-weighted MRI could non-invasively measure bone displacements with random errors below 30 μm, and strains with both systematic and random errors below 0.02% (Tavana et al., 2020). Therefore, we hypothesised that MRI-based DVC might enable clinicians to non-invasively evaluate ankle joint mechanics in clinical settings. The primary objective of this study is to use this optimised MRI-based DVC technique for direct, non-invasive in vivo measurements of the translation of ankle bones, and of joint 3D contact strains under load. Secondly, we want to investigate the potential correlation between the tibiotalar joint contact strains in healthy subjects and the prevalence of OLT anatomical distribution in patients.

2. Methods

Eight ankles from four healthy asymptomatic volunteers (three male and one female, mean age 33 years, ranging from 25 to 54 years old) were examined in this study. A preliminary power analysis was performed using available in vivo ankle kinematics data in the literature to identify the required number of subjects for this study (Peña Fernández et al., 2020). This analysis identified that the sample size of eight ankles can be considered sufficient for the current study. Subjects were excluded from the participation in this study if they had any ongoing ankle pain/instability, apparent abnormalities in the ankle examination, malalignment, or any ankle surgery. Pregnant women were also excluded from this study. The study received ethical approval from the Imperial College Research Ethics Committee (ICREC reference: 17IC4131). All methods were carried out in accordance with relevant guidelines and regulations. Written informed consent was obtained from all participants prior to imaging.

2.1. MR imaging and loading rig

MR imaging was conducted using a 3 T Siemens Magnetom Spectra MRI machine (Siemens Medical Solution, Erlangen, Germany) with a standard 16 channel high-resolution ankle coil (Siemens Medical Solution, Erlangen, Germany). Each ankle was scanned once in an unloaded state and once in a loaded state (50% body weight) using a T1 weighted MRI sequence (echo time (TE) = 12 ms, repetition time (TR) = 700 ms, echo train length = 25, bandwidth = 385, flip angle 120°, echo numbers = 0, number of averages = 0, voxel size = $500 \times 500 \times 500$ μm^3, slice gap = 0%, scan time 3:30 (min:s)) with a 3D fast spin-echo acquisition mode. The findings by Tavana et al. (2020) identified that the T1 weighted sequence is the optimal MR imaging setting to minimise DVC deformation and strain measurement errors in human ankle bones. Both of the unloaded and loaded scans were performed in the supine position (Fig. 1), without any changes in MRI settings between the two scans. An MRI compatible rig was used to apply 50% of the volunteer's body weight to the ankle being imaged (Fig. 1). The loading rig included a resizable inelastic vest securely attached to an adjustable strap (5 cm width) that was predominantly inelastic, but incorporated a small elastic section (32.5 cm length) with stiffness (k) of 110 N/cm. In the unloaded state, there was no tension in the elastic part of the strap that was fitted around the volunteer's heel. However, in the loaded state, 50% of the volunteer's body weight was used to calculate the length by which the strap needed to be shortened, in accordance with the elastic strap's stiffness (k). Since the length of the inelastic strap was reduced (by shortening the inelastic strap), for obtaining the loaded scan, the volunteer had to push and hold the strap at the initial (unloaded) length (by elongating the elastic portion of the strap) during the scanning. To confirm that the applied load to the ankle was equal to 50% of the body weight, the loading rig was calibrated with a loadcell in the laboratory environment on two volunteers (one male and one female). The elongation magnitude of the elastic strap (ΔL) was measured both before and after the scanning to ensure the load level was kept constant during the scan time. These measurements indicated that the pre-scan and post-scan ΔL differences never exceed 0.1 mm (~11 N), which was approximately 3% of the applied load, and deemed low enough to have negligible effect on the outcomes of this study. Additionally, the pre-scan and post-scan ΔL differences in the elastic strap were measured for all ankles during the MRI scanning to ensure this difference did not exceed 0.3 mm (33N), which was considered as the threshold for repeating the MRI scan. To reduce the risk of applying uneven load to the medial and lateral sides of the joint, adjustable inelastic straps were used on the both medial and lateral sides of the ankle (Fig. 1). This risk was further reduced by asking subjects to position themselves such that the load was equally distributed between the left and right sides of their ankle. In order to avoid applying torque to the ankle joint in the sagittal plane and to keep consistency in the location of the applied load among
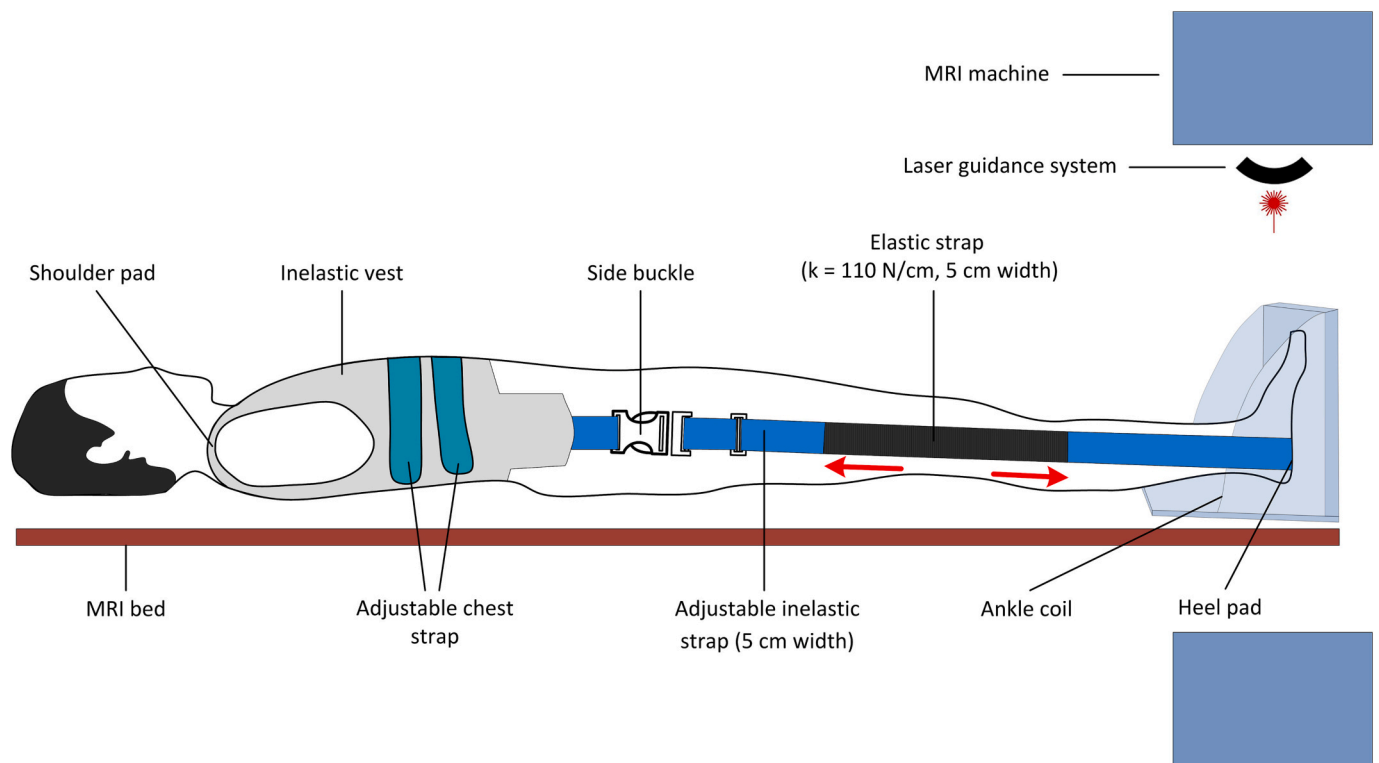
Fig. 1. Schematic diagram of MRI compatible loading rig used for in vivo measurements of ankle kinematics and tibiotalar joint contact strains. 50% of the volunteer's body weight was applied to the ankle by pushing the strap (32.5 cm length and 5 cm width) and elongating the elastic strap.

different subjects, the mid-width line of the loading strap was aligned with the medial malleolus of each ankle. To minimise rigid body movements between the two scans, key anatomic features of the foot such as malleolus and metatarsals were aligned using the laser guidance system that was built into the MRI machine (Fig. 1).

2.2. Image post-processing

Image post-processing was conducted before DVC analysis following a fixed workflow by a single observer (Fig. 2). Each 3D image data set included the distal tibia (30.8 ± 2.9 mm), talus, navicular, and calcaneus (Fig. 2(a)) with 16-bit grey levels. Initially, a sample-specific 3D binary region-of-interest mask was created for each bone individually and later for the tibiotalar and subtalar joints of each ankle (Fig. 2(b)) by semi-automatic segmentation, using Mimics (Materialise HQ, v.19.0, Leuven, Belgium). These masks were used to exclude surrounding tissues (bone and other soft tissues) from the DVC analysis, ensuring that only the selected tissue was analysed. Segmentation of individual bones allowed the kinematics of each bone to be calculated separately and segmentation of the tibiotalar joint allowed cartilage contact strains to be calculated. Afterwards, rigid body movement of the whole foot between the two scans was corrected using surface-based registration in two steps. In the first step, both MR images were imported into a three-dimensional environment (Fig. 2(c) - left), and the position of each MRI was individually manipulated in six degrees of freedom to manually match the outlines of the volume surfaces. In the second step, automatic rigid registration was conducted (Fiji 1.53c, National Health Institute, Bethesda, MD, USA) based on an iterative, multivariate, optimisation algorithm that minimises the Euclidean distance (corresponding to the square root of summed squares of voxel intensity differences) between the two scans (Schmid, 2010). The calculated transformation matrix (three translational and three rotational parameters) between the two scans was then applied to the target image to correct rigid body movement, resulting in an optimal match of the outer surface of the ankles

from both MRIs (Fig. 2 (d)). Finally, a left-handed orthogonal coordinate system was created on the anterior-distal corner of the first medial slice. For both left and right ankles, the positive x-direction was directed posteriorly, the positive y-direction proximally, and the positive z-direction laterally (Fig. 2(b)). In anteroposterior translations, the negative values define anterior translations, in mediolateral translations, the negative values identify medial translations, and in superoinferior translations, the negative values define inferior translations.

2.3. Kinematics and contact strain measurements

DVC analysis (DaVis 8.4.0, LaVision, Goettingen, Germany) was conducted on the obtained MR images to calculate the 3D displacement fields of the talus, tibia, and calcaneus from the unloaded state to the loaded state. DVC was also used to compute 3D contact strains at the tibiotalar joint under 50% of body weight. In a previous study (Tavana et al., 2020) we have shown that the combination of Fast Fourier Transform (FFT), and Direct Correlation (DC) approach (FFT + DC), is the optimal DVC setting for this application and can provide a notably lower displacement and strain measurement error in comparison with separate FFT or DC approaches applied on their own. The FFT + DC approach implements a predictor-corrector technique that uses the FFT approach for an initial prediction of large displacements, which are then refined using the DC approach. DVC analysis was conducted using a single-pass scheme with a subset size of $16 \times 16 \times 16$ voxels and 50% overlap (4 mm^3). By using this subset size, displacements can be measured with random errors below 30 μm, and strains can be calculated with both systematic and random errors below 0.02% (Tavana et al., 2020). After obtaining the displacement fields, vector post-processing was carried out to detect and remove spurious vectors and outliers close to the boundary of masks, by using an adapted particle image velocimetry (PIV) outlier detection technique (removal threshold = 2, kernel size $5 \times 5 \times 5$, ε = 0.1). This technique is described in more detail by Westerweel and Scarano (2005).
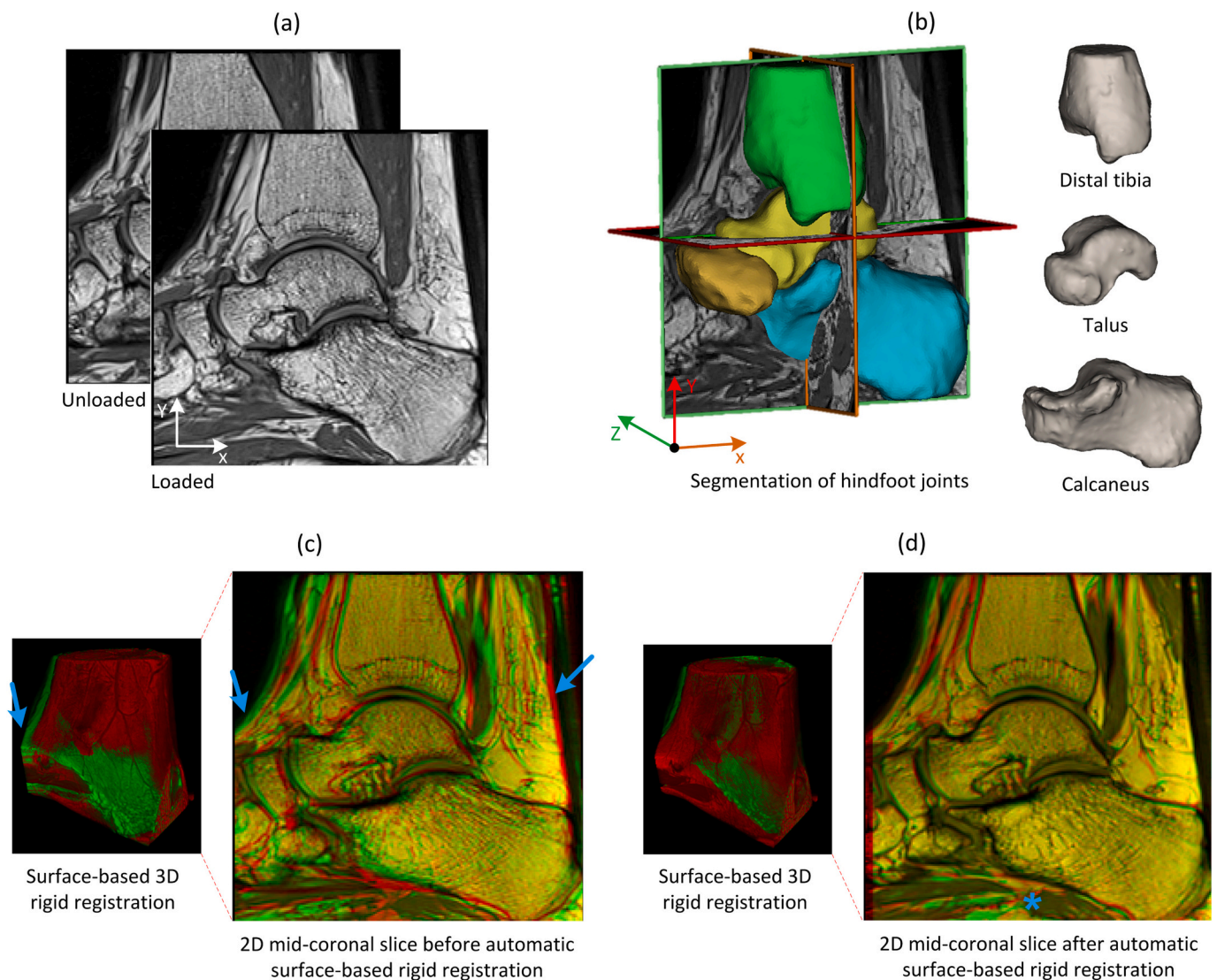
Fig. 2. Workflow of the imaging and image post-processing: (a) MR images were obtained from each volunteer's ankle in an unloaded and loaded state (50% body weight) using a 3 T MRI machine and T1 weighted sequence. (b) Segmentation of the distal tibia, talus, and calcaneus was performed to generate a 3D anatomic model of the ankle. (c) Volumetric MR images in the unloaded state (red pixels) superimposed on the loaded state (green pixels) were imported into a 3D environment to evaluate rigid body movement of the whole foot between the two states and to conduct manual registration, blue arrows point to the mismatch (rigid body movement). (d) Rigid body movement between the two states was corrected using an optimisation, iterative algorithm. When pixels of the unloaded and the loaded states were optimally matched, the pixels became yellow. The asterisk denotes a mismatch at the sole of the foot caused by the non-rigid deformations. (For interpretation of the references to colour in this figure legend, the reader is referred to the web version of this article.)

The refined displacement vectors obtained from DVC analysis were extracted from DaVis and imported to a custom written MATLAB script (MathWorks, Inc., Natick, MA) to calculate all components of the Green-Lagrange strain using a centered finite differences scheme. The contact strains that were calculated at the tibiotalar joint were projected into a 9-zone anatomical grid system (Fig. 3) previously developed by (Raikin et al., 2007), using a custom written MATLAB script. Raikin et al. (2007) developed a 9-zone anatomical grid system in order to standardise localisation of OLTs on the talar dome, as depicted in Fig. 3. This system has since been widely used for this application (Raikin et al., 2007; van Diepen et al., 2020). In this study, the gridding system was used to visualise strain distribution over different anatomical regions of the talar dome so that a more precise comparison of strain distribution with future studies of this nature could be made. The primary outcome measure of this study was the 3D calculation of ankle joint kinematics and tibiotalar joint contact strains. The secondary outcome measure was to investigate potential correlations between the tibiotalar joint contact strains and distributions of OLTs in the human ankle joint.

Throughout the manuscript, one-way repeated measures analysis of variance (ANOVA) with Tukey post-hoc tests were implemented to identify differences in translations between the tibia, talus, and calcaneus using SPSS statistics 25 (IBM corp., Armonk, NY). Paired-samples *t*-test was used to determine differences between the kinematics of the left and right ankles. A Shapiro-Wilk's test was implemented to assess normality in all statistical analyses, and a Levene's test was conducted to determine whether the assumption of homogeneity of variance was legitimate. A measure of effect size (Cohen's d) (Cohen, 1988) and power calculation were performed using G*Power (HeinrichHeine-Universitat Düsseldorf, Germany) (Faul et al., 2007) to identify the required number of subjects for this study and to investigate the effect of sample size on the outcome of statistical analysis.

3. Results

Using DVC with a subset size of 4 mm resulted in an average of 527 measurement points in the tibia, 514 measurement points in the talus,
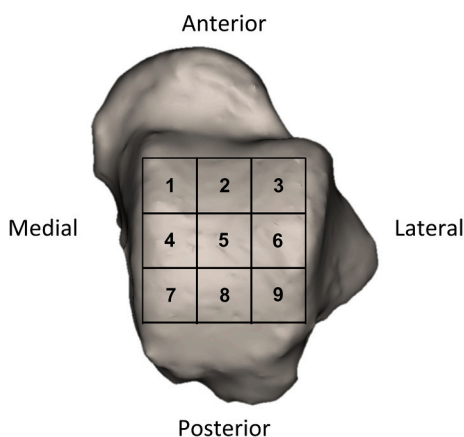
Fig. 3. The anatomical 9-zone grid system developed by Raikin et al. (2007) illustrated on the talar dome. The articular surface of talar dome was divided into nine zones with equal area in an axial plane by using two vertical and two horizontal lines. Numerical identifiers were assigned to the nine zones, with zones 1, 2, and 3 positioned on the anterior talus, and zones 3, 6, and 9 positioned laterally. Zone 5 is defined as the central zone and zone 7 is the most posterior medial zone.

and 912 measurement points in the calcaneus. Additionally, this subset size resulted in an average of nine measurement points within each zone of the 9-zone anatomical grid system. The displacement vectors obtained from the DVC analysis were used to calculate the average total 3D translation, anteroposterior translation, mediolateral translation, and superoinferior translation of the tibia, talus, and calcaneus.

3.1. Total three-dimensional translation

The total 3D translations of the tibia, talus, and calcaneus were measured between the unloaded and loaded states (Fig. 4). The total 3D translation was significantly different between different ankle bones ($p < 0.05$). On average, the total translation of the calcaneus in 3D was smaller (0.48 ± 0.15 mm, $p < 0.05$) than the tibia (0.93 ± 0.16 mm, $d = 2.90$, *Power 0.99*) and the talus (1.03 ± 0.26 mm, $d = 2.59$, *Power 0.98*), and no significant difference ($p > 0.05$) was observed between the mean 3D translation of the tibia and the talus (Fig. 5(a)). In all subjects, the

largest displacements in the talus were observed in the talar neck and head (Fig. 4). On average, the absolute differences observed between the total 3D translations of the left and right ankles within subjects was 0.26 ± 0.11 mm for tibia, 0.34 ± 0.31 mm for talus, 0.13 ± 0.12 mm for calcaneus. The total 3D translations of the left tibia were significantly larger ($p < 0.05$) than the right tibia; however, no differences ($p > 0.05$) were observed in the total 3D translations of talus and calcaneus between the left and right ankles (Fig. 6(a)).

3.2. Anteroposterior translation

The anteroposterior translation was significantly different between different ankle bones ($p < 0.05$). Under the applied load, significant differences ($p < 0.0001$, $d > 4.19$, *Power > 0.99*) were found in the anteroposterior translation of the talus when compared to the translation in both the tibia and calcaneus. All eight tali translated anteriorly, by on average 0.52 ± 0.18 mm. However, the tibia and the calcaneus translated posteriorly by an average of 0.24 ± 0.28 mm and 0.09 ± 0.10 mm, respectively (Fig. 5(b)). No statistically significant difference was found between the posterior movement of the tibia and the calcaneus ($p > 0.05$). On average, the absolute differences observed between the anteroposterior translations of the left and right ankles within subjects was 0.28 ± 0.17 mm for tibia, 0.24 ± 0.18 mm for talus, 0.12 ± 0.08 mm for calcaneus. No differences ($p > 0.05$) were observed in the anteroposterior translation of tibia, talus, and calcaneus between the left and right ankles (Fig. 6(b)).

3.3. Mediolateral translation

The mediolateral translation was significantly different between different ankle bones ($p < 0.05$). The mediolateral translation was statistically different ($p = 0.01$, $d = 1.42$, *Power 0.88*) between the tibia and the talus from the unloaded to the loaded state (Fig. 5(c)). The talus displaced medially by an average of 0.38 ± 0.30 mm, whereas the tibia translated laterally by 0.14 ± 0.42 mm. The average of mediolateral movements among all the calcaneus was slightly lateral by a mean translation of 0.05 ± 0.22 mm, which ranged from 0.19 mm medial translation to 0.50 mm lateral translation. There was no significant difference ($p > 0.05$) in mediolateral translation of the calcaneus when compared to either the talus or the tibia (Fig. 5(c)). On average, the absolute differences observed between the mediolateral translations of
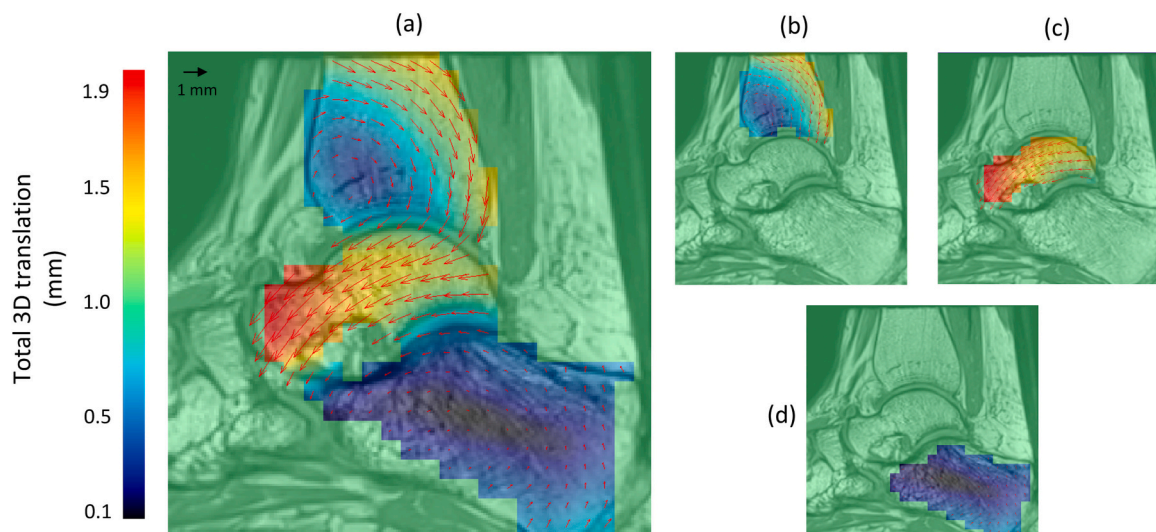

Fig. 4. Total 3D displacement from the unloaded state to the loaded state computed using DVC (a). Subject-specific 3D binary masks were generated to calculate the translations of the tibia (b), the talus (c), and the calcaneus (d) individually. Red vectors identify the total displacements. For the purpose of better visualization, in 2D views (a,c,d) the vectors are magnified by a factor of five. Vector reference is identified in (a). (For interpretation of the references to colour in this figure legend, the reader is referred to the web version of this article.)
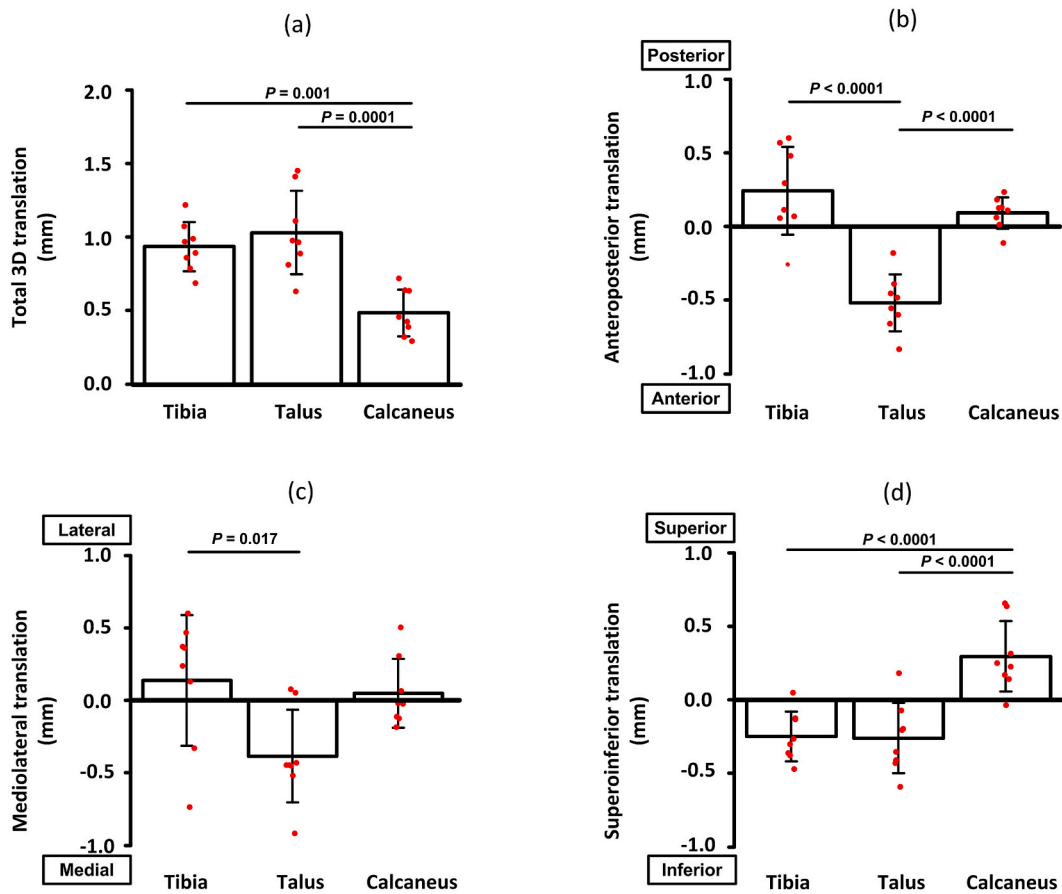
Fig. 5. Bar plots of the total 3D translations (a), anteroposterior translations (b), mediolateral translations (c), and superoinferior translations (d) for the tibia, talus, and calcaneus. The bars and error bars represent the average and standard deviation of translation values, respectively.
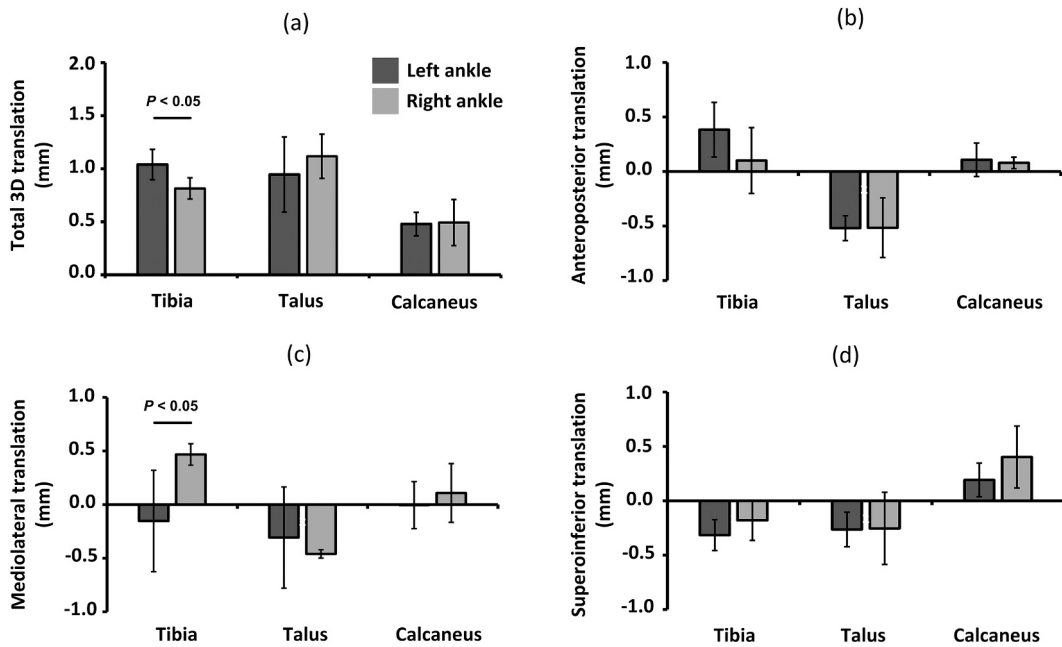

Fig. 6. Bar plots of the total 3D translations (a), anteroposterior translations (b), mediolateral translations (c), and superoinferior translations (d) for the tibia, talus, and calcaneus of the left and right ankles. The bars and error bars represent the average and standard deviation of translation values, respectively.

the left and right ankles within subjects was 0.61 ± 0.38 mm for tibia, 0.36 ± 0.23 mm for talus, 0.28 ± 0.21 mm for calcaneus. A significant difference ($p < 0.05$) was found between the mediolateral translation of the left and right tibia; however, no differences ($p > 0.05$) were observed in the mediolateral translation of talus and calcaneus between the left and right ankles (Fig. 6(c)).

3.4. Superoinferior translation

The superoinferior translation was significantly different between different ankle bones ($p < 0.05$). When going from the unloaded state to the loaded state, significant differences ($p < 0.0001$, $d > 2.86$, *Power > 0.99*) were detected between the superoinferior translation of the calcaneus when compared to both the tibia and the talus (Fig. 5(d)). The calcaneus translated superiorly by the average of 0.30 ± 0.22 mm, whereas the tibia and the talus displaced inferiorly by 0.25 ± 0.16 mm and 0.26 ± 0.22 mm, respectively. No superoinferior translation difference ($p > 0.05$) was seen between the tibia and the talus (Fig. 5(d)). On average, the absolute differences observed between the superoinferior translations of the left and right ankles within subjects was 0.14 ± 0.16 mm for tibia, 0.29 ± 0.25 mm for talus, 0.33 ± 0.27 mm for calcaneus. No differences ($p > 0.05$) were observed in the superoinferior translation of tibia, talus, and calcaneus between the left and right ankles (Fig. 6(d)).

3.5. Tibiotalar joint contact strains

The ankle joint contact strains were calculated using non-rigid DVC analysis on the 3D reconstructed MR images (Fig. 7). The DVC-measured contact strain at the tibiotalar joint was projected onto the 9-zone anatomical grid system. The average peak axial strain (ε_{yy}) over the talar dome was $-5.06 \pm 2.31\%$ (Fig. 8(a)). In all ankle joints ($n = 8$), the site of peak axial strains were commonly found in the posterior part of the talar dome, with three peaks in the posteromedial (zone 7), three peaks in posterolateral (zone 9), one peak in posterocentral (zone 8), and one peak in the centromedial (zone 4) region (Fig. 8(b)). The average of the peak of minimum principal strains (maximum compression) in the talar dome was $-7.04 \pm 2.18\%$ (Fig. 8(c)). Although one peak (minimum principal strains) was found in the posterocentral area (zone 8), the areas found to have the highest strains were the medial and lateral zones (zones 1, 4, 6, and 9) (Fig. 8(d)).

The average of the peak of the maximum principal strains (maximum

Fig. 7. Minimum 3D principal strain distribution in the tibia, talus, calcaneus, tibiotalar joint, and subtalar joint superimposed on the mid-coronal slice of a typical ankle.

tension) in the talar dome was $6.95 \pm 2.33\%$ (Fig. 9(a)). Seven out of eight of the peak strains were in the medial area of the talar dome (Fig. 9(b)), with three in the anteromedial (zone 1), three in the posteromedial areas (zone 7), and one in centromedial (zone 4) regions. The remaining one peak was found to be in the anterocentral (zone 2) region. In the talar dome, the average of the maximum 3D shear strain, was $6.41 \pm 2.34\%$ (Fig. 9(c)). Three and four of the peak shear strains were found in the medial (zones 1 and 4) and lateral (zones 3 and 9) aspects of the talar dome, respectively, and only one peak was in the anterocentral (zone 2) region (Fig. 9(d)).

4. Discussion

In this study, we used DVC combined with clinical MRI as a non-invasive technique to quantify the in vivo ankle kinematics and the tibiotalar joint contact strains. Previously, it was identified that even in pure axial loading, joints experience large compressive and shear strains due to complex rigid body motions (Chan et al., 2016). Hence, it has been suggested that the evaluation of the principal and shear strains are required for better understanding of the overall strain environment within the joint. The present study is the first to use DVC in combination with clinical MRI to measure kinematics and 3D strain components in vivo within the human ankle joint. The imaging parameters and DVC settings were optimised for this specific in vivo measurement, establishing a framework that can be used in future studies implementing this technique.

Medical imaging techniques that calculate tissue morphology alone may not provide direct information regarding the mechanical behaviour of the tissue, and cannot detect biomechanical changes that can lead to tissue damage and early-stage degeneration (Griebel et al., 2014; Subburaj et al., 2012). Therefore, in vivo evaluation of ankle joint mechanics could aid clinicians to define optimal patient-specific treatment. The proposed technique in this study is non-invasive, does not involve any radiation exposure, and does not require complex hardware that is not readily available in a hospital setting. These advantages overcome some of the main limitations of the previously developed kinematics and strain measurement techniques (Caputo et al., 2009; Peña Fernández et al., 2020), which increases its suitability for clinical adaption.

As expected, the ankle bones displayed complex and non-identical movements relative to each other (Fig. 4 and Fig. 5), with approximately two times larger ($p \leq 0.001$) total 3D translation of the tibia and the talus, compared with the calcaneus (Fig. 5(a)). Generally, a high level of consistency was observed among ankle movements of different subjects. Our findings have shown that under compressive load, the talus translates anteriorly (Fig. 5(b)), which is in line with the findings of previous in vivo studies that used computational models based on dual fluoroscopy to capture the joint kinematics (Caputo et al., 2009; Roach et al., 2016). Under 50% of body weight Caputo et al. (2009) measured talus anterior movement of 0.3 ± 0.6 mm (mean $\pm$ SD), which is similar to those found in the present study (0.52 ± 0.18 mm). Significant differences ($p \leq 0.001$) in anteroposterior movements of the talus in comparison with both the tibia and the calcaneus were observed in this study (Fig. 5(b)), which may explain the generation of shear strains and increased wear on the tibiotalar joint caused by anterior movement of the talus (Taga et al., 1993). Under 50% of body weight, Caputo et al. (2009) observed slight lateral (0.1 ± 0.6 mm) and slight superior (0.1 ± 0.7 mm) translation of the talus, which differed somewhat from those seen in this study (modest medial (0.38 ± 0.30 mm) and inferior (0.26 ± 0.22 mm) translations). This may be a result of the different loading conditions used in these studies. In the Caputo et al. (2009) study, volunteers contracted their muscles to maintain balance and stood with 50% of their body weight on a force plate within the beams of fluoroscopes, and the in vivo ankle loads mainly included ground reaction and gravitational forces. However, in the present study, volunteers loaded their ankle by intensively contracting their muscles (internal muscle force) and elongating the elastic straps (strap reaction force) (Fig. 1),
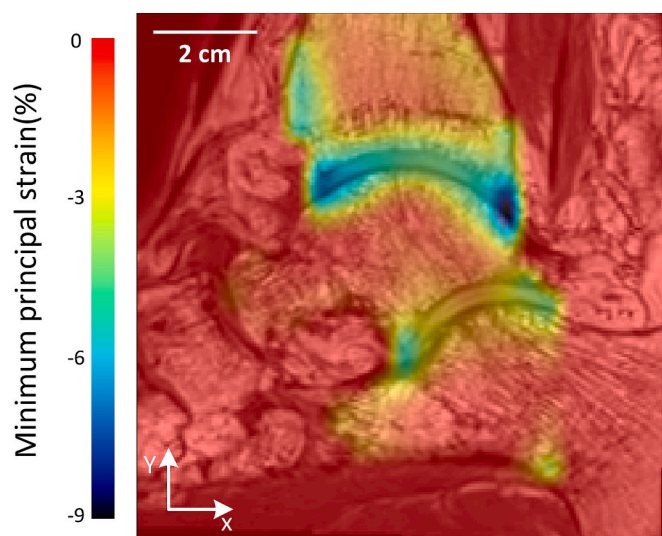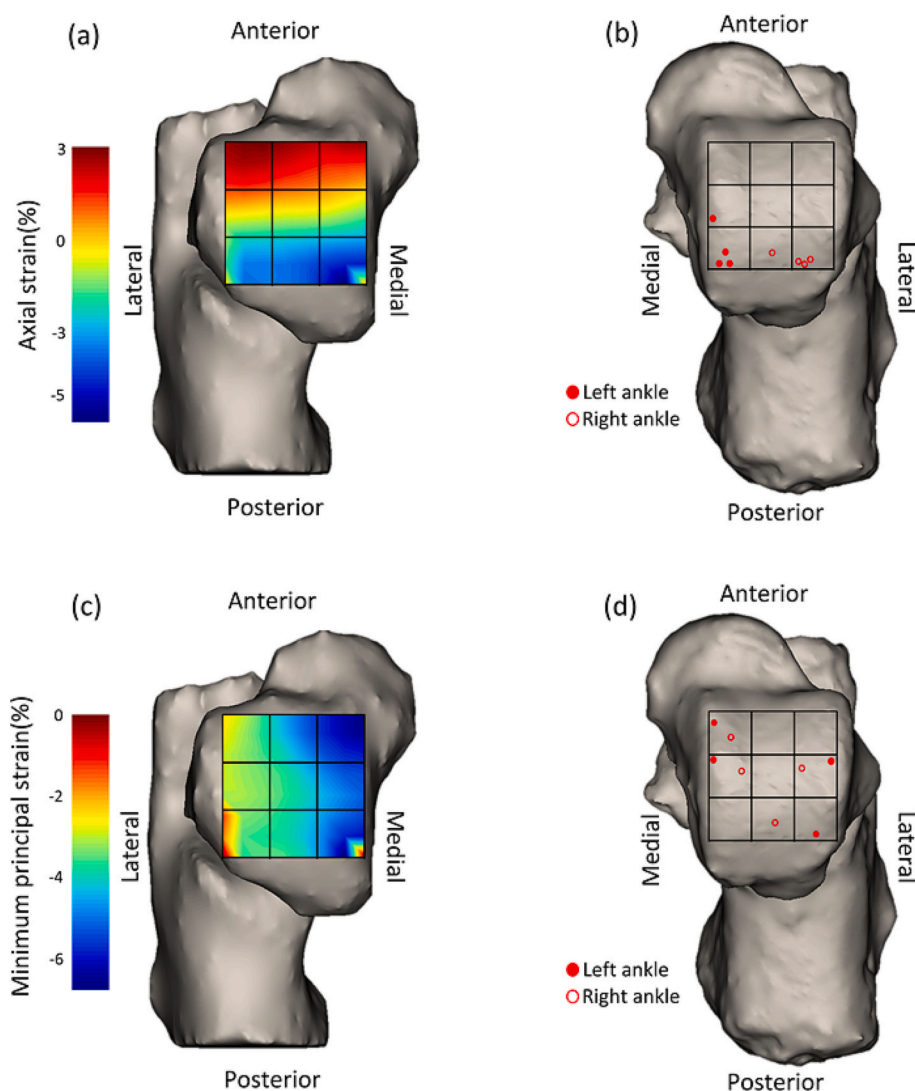
Fig. 8. The distribution of axial (ε_{yy}) strain (a) and minimum 3D principal (maximum compression) strain (c) over the talar dome projected onto the 9-zone anatomical grid system for a typical subject. The location distribution of the peak axial (ε_{yy}) strain (b) and minimum 3D principal (maximum compression) strain (d) from all eight subjects on the 9-zone anatomical grid system. In (b) and (d) solid points define the locations of peak strains for the left ankle, and hollow points represent the locations of peak strains for the right ankle.

which resulted in inferior translations of both the talus and the tibia (Fig. 5(d)).

The average peak maximum tensile, compressive, and shear strains for the tibiotalar joint under 50% of the body weight were calculated as $6.95 \pm 2.33\%$, $-7.04 \pm 2.18\%$, and $6.41 \pm 2.34\%$, respectively. The obtained contact strains in this study were similar to those physiologic strain magnitudes measured in articular cartilage of the healthy joints under static loading, which ranged from 2% to 9% (Davis et al., 2021; Sanchez-Adams et al., 2014; Steinmetz et al., 2015). The distribution of peak strains over the tibiotalar joint in the present study may explain the distribution of OLTs in the talus observed in previous studies (Dahmen et al., 2018; Raikin et al., 2007; van Diepen et al., 2020). Raikin et al. (2007) evaluated the distribution of 428 OLTs on the talar dome, and found 62.9% of lesions were located medially, 3.7% of lesions were located centrally, and 33.4% of lesions were located laterally. A similar distribution pattern was observed by Dahmen et al. (2018), who found 77% of lesions were medial, 2% were central, and 21% were lateral. Additionally, a recent systematic review (van Diepen et al., 2020) assessed the location distribution of 2087 OLTs and reported that 69%, 7%, and 24% of the OLTs were found in the medial, central and lateral regions, respectively. Our findings showed that 87.5% of the peak ankle joint contact strains (peak tensile, compressive and shear strains) were localized at the medial and lateral zones of the talar dome which could suggest anatomical predisposition of these regions to developing

osteochondral lesions especially in the presence of ankle instability as demonstrated by various clinical studies (Dahmen et al., 2018; Raikin et al., 2007; van Diepen et al., 2020). On top of that, the evaluation of strain distribution over the talar dome utilizing the 9-zone grid provides a more standardized scheme for clinicians to correlate sites of strain concentration to clinical findings of OLT.

Previous studies have shown that the anterior tibiofibular ligament (ATFL) plays an important role in resisting anterior translation of the talus (Hollis et al., 1995; Hubbard, 2008; Jones et al., 2007; Löfvenberg et al., 1994), and that ATFL insufficiency causes a significant increase in anterior translation of the talus (Caputo et al., 2009), which may predispose it to OLTs (Taga et al., 1993). Taga et al. (1993) reported in >89% of patient with injured lateral ligaments, OLTs were found in the anteromedial region of the tibiotalar joint, and they hypothesised that there is a link between kinematic alterations and OLTs development. Other studies (Harrington, 1979; Hintermann et al., 2002) observed lateral ankle sprains and ligament injuries significantly increase wear on the medial region of the tibiotalar joint, possibly due to the increased contact stresses in this region. Anatomical differences among patients could also be a risk factor, and may affect the mechanism of OLT development by altering load distributions over the talar dome (Nakasa et al., 2018). Recently, Hong and Calder (2022) reported on a series of 147 elite athletes' ability to return to sports after early lateral ligament repair of the ankle and found that there were only 6.8% of patients with
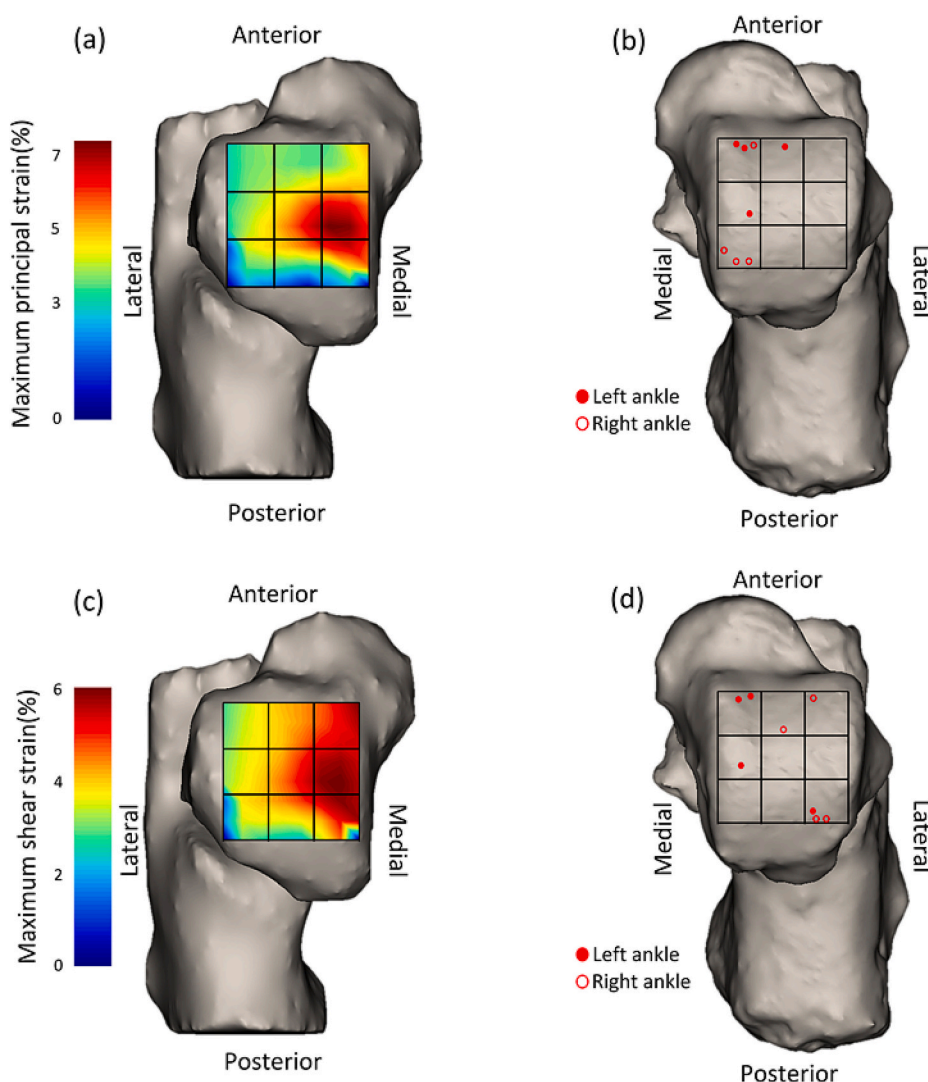
Fig. 9. The distribution of maximum 3D principal (maximum tension) strain (a) and maximum 3D shear strain (c) over the talar dome projected onto the 9-zone anatomical grid system for a typical subject. The location distribution of the peak maximum 3D principal (maximum tension) strain (b) and maximum 3D shear strain (d) from all eight subject on the 9-zone anatomical grid system. In (b) and (d) solid points define the locations of peak strains for the left ankle, and hollow points represent the locations of peak strains for the right ankle.

OLT compared to the literature ranging from 24% to 55%. They suggested that this notable difference is because the existing literature reviewed patients with chronic lateral ligament instability while their cohort of patients had acute lateral ligament injury. Hence, the authors posit that early lateral ligament repair for Grade III instability restores the ankle stability and may potentially protect the cartilage from repetitive injury due to chronic instability and the restoration of ankle stability yielded a re-injury rate of 2% in their series. Therefore, it is apparent that this direct in vivo evaluation of contact strains at the tibiotalar joint adds to the current body of knowledge by illustrating the increased strains on medial and lateral zones of the talus which could be a risk factor to developing osteochondral lesions in cases of ankle instability or malalignments. Clinically, this information is pertinent for Orthopaedic and Sports Surgeons as it further highlights the importance of restoring ankle joint congruency, mechanical alignment and ankle stability to equalize load distributions over the ankle joint during surgical interventions. Additionally, clinicians can also utilize this MRI-DVC technique as a non-invasive assessment tool to monitor potential development of excessive contact stresses in patients with non-surgically treated ankle lateral ligament instability. Through this, the need for whether surgical intervention can be performed earlier or the adequacy of a particular surgical intervention (new ligament repair or reconstruction technique) in restoring normal joint contact strains can be assessed.

This study has some limitations that should be acknowledged.

Firstly, there was a limited number of volunteers that participated in this study ($n = 8$ ankles, four participants). Although statistical power was measured to ensure the sample size of 8 ankles was adequate to support the significant differences presented, the fact that it was from 4 individuals means generalisation of both the measured kinematics and the location of peak strains in the 9-zone grid system warrants further investigations with larger sample sizes. Additionally, the loading scheme in this study was different from those experienced by the ankle during daily activities. Due to the inherent limitation of conventional MRI machines, volunteers were scanned in the supine position, and were not subjected to gravitational loads. Future studies can implement this technique in combination with clinical weight-bearing upright MRI (Alyas et al., 2008) to overcome this limitation. Although care was taken during the placement of the loading strap to avoid applying torque to the ankle joint in the sagittal plane, micro-movement of the loading strap may have caused a small amount of rotational moment in the sagittal plane, which should be considered while interpreting the findings of this study. Finally, in this study, the joint kinematics and contact strains were only quantified for pure axial compression under quasi-static loading, which limited the generalisability of the findings of this study. Although axial compression is the major load direction when standing, to better understand the joint mechanics, future studies should extend this analysis to investigate other static loading conditions such as plantarflexion, dorsiflexion, inversion, and eversion. The proposed MRI-DVC approach is not able to quantify ankle joint mechanics during

dynamic loading modalities. Combining the DVC technique used in this study with real-time MRI (Draper et al., 2009) may provide dynamic information of joint kinematics and strains, and can be also considered for future studies.

5. Conclusion

This work demonstrated the feasibility of using clinical MRI-DVC as a novel non-invasive tool for in vivo evaluation of joint mechanics. Clinical MRI-DVC can provide data that can be used to describe the baseline mechanical behaviour of healthy joints, help clinicians to restore normal joint contact strains, and monitor the effectiveness of surgical interventions. The findings of this study determined that the medial and lateral regions of the talar dome experience higher tensile, compressive and shear strains, which has shown a possible link between the site of strain concentrations and the distribution of OLTs in the event of ankle instability or malalignment.

Funding

CRediT authorship contribution statement

Saman Tavana: Conceptualization, Methodology, Software, Formal analysis, Visualization, Writing – original draft, Project administration, Writing – review & editing. **Jeffrey N. Clark:** Methodology, Investigation, Software, Visualization, Writing – review & editing. **Choon Chiet Hong:** Methodology, Investigation, Writing – review & editing. **Nicolas Newell:** Methodology, Investigation, Formal analysis, Writing – review & editing. **James D. Calder:** Conceptualization, Methodology, Investigation, Resources, Writing – review & editing. **Ulrich Hansen:** Conceptualization, Methodology, Investigation, Resources, Writing – review & editing, Supervision.

Declaration of Competing Interest

The authors declare that they have no known competing financial interests or personal relationships that could have appeared to influence the work reported in this paper.

Acknowledgements

References

Alyas, F., Connell, D., Saifuddin, A., 2008. Upright positional MRI of the lumbar spine. Clin. Radiol. 63, 1035–1048.

Arndt, A., Westblad, P., Winson, I., Hashimoto, T., Lundberg, A., 2004. Ankle and subtalar kinematics measured with intracortical pins during the stance phase of walking. Foot Ankle Int. 25, 357–364.

Arndt, A., Wolf, P., Nester, C., Liu, A., Jones, R., Howard, D., Stacoff, A., Lundgren, P., Lundberg, A., 2006. Intrinsic foot motion measured in vivo during barefoot running. J. Biomech. 39, S182.

Bauman, J.M., Chang, Y.H., 2010. High-speed X-ray video demonstrates significant skin movement errors with standard optical kinematics during rat locomotion. J. Neurosci. Methods 186, 18–24.

Beimers, L., Maria Tuijthof, G.J., Blankevoort, L., Jonges, R., Maas, M., van Dijk, C.N., 2008. In-vivo range of motion of the subtalar joint using computed tomography. J. Biomech. 41, 1390–1397.

Bischof, J.E., Spritzer, C.E., Caputo, A.M., Easley, M.E., DeOrio, J.K., Nunley, J.A., DeFrate, L.E., 2010. In vivo cartilage contact strains in patients with lateral ankle instability. J. Biomech. 43, 2561–2566.

Caputo, A.M., Lee, J.Y., Spritzer, C.E., Easley, M.E., DeOrio, J.K., Nunley, J.A., DeFrate, L.E., 2009. In vivo kinematics of the tibiotalar joint after lateral ankle instability. Am. J. Sports Med. 37, 2241–2248.

Chan, D.D., Cai, L., Butz, K.D., Trippel, S.B., Nauman, E.A., Neu, C.P., 2016. In vivo articular cartilage deformation: noninvasive quantification of intratissue strain during joint contact in the human knee. Sci. Rep. 6, 19220.

Cohen, J., 1988. Statistical Power Analysis for the Behavioral Sciences. L. Erlbaum Associates, Hillsdale, N.J.

Dahmen, J., Lambers, K.T.A., Reilingh, M.L., van Bergen, C.J.A., Stufkens, S.A.S., Kerkhoffs, G.M.M.J., 2018. No superior treatment for primary osteochondral defects of the talus. Knee Surg. Sports Traumatol. Arthrosc. 26, 2142–2157.

Davis, S., Roldo, M., Blunn, G., Tozzi, G., Roncada, T., 2021. Influence of the mechanical environment on the regeneration of osteochondral defects. Front. Bioeng. Biotechnol. 9.

Dettwyler, M., Stacoff, A., Kramers-de Quervain, I.A., Stüssi, E., 2004. Modelling of the ankle joint complex. Reflections with regards to ankle prostheses. Foot Ankle Surg. 10, 109–119.

Di Marco, R., Rossi, S., Racic, V., Cappa, P., Mazzà, C., 2016. Concurrent repeatability and reproducibility analyses of four marker placement protocols for the foot-ankle complex. J. Biomech. 49, 3168–3176.

Draper, C.E., Besier, T.F., Santos, J.M., Jennings, F., Fredericson, M., Gold, G.E., Beaupre, G.S., Delp, S.L., 2009. Using real-time MRI to quantify altered joint kinematics in subjects with patellofemoral pain and to evaluate the effects of a patellar brace or sleeve on joint motion. J. Orthop. Res. 27, 571–577.

Fassbind, M.J., Rohr, E.S., Hu, Y., Haynor, D.R., Siegler, S., Sangeorzan, B.J., Ledoux, W. R., 2011. Evaluating foot kinematics using magnetic resonance imaging: from maximum plantar flexion, inversion, and internal rotation to maximum dorsiflexion, eversion, and external rotation. J. Biomech. Eng. 133.

Faul, F., Erdfelder, E., Lang, A.-G., Buchner, A., 2007. G*power 3: a flexible statistical power analysis program for the social, behavioral, and biomedical sciences. Behav. Res. Methods 39, 175–191.

Gorton 3rd, G.E., Hebert, D.A., Gannotti, M.E., 2009. Assessment of the kinematic variability among 12 motion analysis laboratories. Gait Posture 29, 398–402.

Goto, A., Moritomo, H., Itohara, T., Watanabe, T., Sugamoto, K., 2009. Three-dimensional in vivo kinematics of the subtalar joint during dorsi-plantarflexion and inversion–eversion. Foot Ankle Int. 30, 432–438.

Griebel, A.J., Trippel, S.B., Emery, N.C., Neu, C.P., 2014. Noninvasive assessment of osteoarthritis severity in human explants by multicontrast MRI. Magn. Reson. Med. 71, 807–814.

Guettler, J.H., Demetropoulos, C.K., Yang, K.H., Jurist, K.A., 2004. Osteochondral defects in the human knee: influence of defect size on cartilage rim stress and load redistribution to surrounding cartilage. Am. J. Sports Med. 32, 1451–1458.

Harrington, K.D., 1979. Degenerative arthritis of the ankle secondary to long-standing lateral ligament instability. J. Bone Joint Surg. Am. 61, 354–361.

Hintermann, B., Boss, A., Schäfer, D., 2002. Arthroscopic findings in patients with chronic ankle instability. Am. J. Sports Med. 30, 402–409.

Hirose, K., Murakami, G., Minowa, T., Kura, H., Yamashita, T., 2004. Lateral ligament injury of the ankle and associated articular cartilage degeneration in the talocrural joint: anatomic study using elderly cadavers. J. Orthop. Sci. 9, 37–43.

Hollis, J.M., Blasier, R.D., Flahiff, C.M., Hofmann, O.E., 1995. Biomechanical comparison of reconstruction techniques in simulated lateral ankle ligament injury. Am. J. Sports Med. 23, 678–682.

Hong, C.C., Calder, J., 2022. Ability to return to sports after early lateral ligament repair of the ankle in 147 elite athletes. Knee Surg. Sports Traumatol. Arthrosc. https://doi. org/10.1007/s00167-022-07270-2.

Hubbard, T.J., 2008. Ligament laxity following inversion injury with and without chronic ankle instability. Foot Ankle Int. 29, 305–311.

Jones, A.P., Sidhom, S., Sefton, G., 2007. A minimally invasive surgical technique for augmented reconstruction of the lateral ankle ligaments with woven polyester tape. J. Foot Ankle Surg. 46, 416–423.

Li, G., Wan, L., Kozanek, M., 2008. Determination of real-time in-vivo cartilage contact deformation in the ankle joint. J. Biomech. 41, 128–136.

Löfvenberg, R., Kärrholm, J., Ahlgren, O., 1994. Ligament reconstruction for ankle instability. A 5-year prospective RSA follow-up of 30 cases. Acta Orthop. Scand. 65, 401–407.

Lundberg, A., Svensson, O.K., 1993. The axes of rotation of the talocalcaneal and talonavicular joints. Foot 3, 65–70.

Mahesh, M., 2001. Fluoroscopy: Patient Radiation Exposure Issues. RadioGraphics 21, 1033–1045.

Montefiori, E., Modenese, L., Di Marco, R., Magni-Manzoni, S., Malattia, C., Petrarca, M., Ronchetti, A., de Horatio, L.T., van Dijkhuizen, P., Wang, A., Wesarg, S., Viceconti, M., Mazzà, C., 2019. An image-based kinematic model of the tibiotalar and subtalar joints and its application to gait analysis in children with juvenile idiopathic arthritis. J. Biomech. 85, 27–36.

Nakasa, T., Sawa, M., Ikuta, Y., Yoshikawa, M., Tsuyuguchi, Y., Adachi, N., 2018. Anatomic feature of deltoid ligament attachment in posteromedial osteochondral lesion of talar dome. J. Orthop. Sci. 23, 377–382.

Nichols, J.A., Roach, K.E., Fiorentino, N.M., Anderson, A.E., 2017. Subject-specific axes of rotation based on talar morphology do not improve predictions of tibiotalar and subtalar joint kinematics. Ann. Biomed. Eng. 45, 2109–2121.

Ogilvie-Harris, D.J., Gilbart, M.K., Chorney, K., 1997. Chronic pain following ankle sprains in athletes: the role of arthroscopic surgery. Arthroscopy 13, 564–574.

O'Loughlin, P.F., Heyworth, B.E., Kennedy, J.G., 2010. Current concepts in the diagnosis and treatment of osteochondral lesions of the ankle. Am. J. Sports Med. 38, 392–404.

Peña Fernández, M., Hoxha, D., Chan, O., Mordecai, S., Blunn, G.W., Tozzi, G., Goldberg, A., 2020. Centre of rotation of the human subtalar joint using weight-bearing clinical computed tomography. Sci. Rep. 10, 1035.

Raikin, S.M., Elias, I., Zoga, A.C., Morrison, W.B., Besser, M.P., Schweitzer, M.E., 2007. Osteochondral lesions of the talus: localization and morphologic data from 424 patients using a novel anatomical grid scheme. Foot Ankle Int. 28, 154–161.

Roach, K.E., Wang, B., Kapron, A.L., Fiorentino, N.M., Saltzman, C.L., Bo Foreman, K., Anderson, A.E., 2016. In vivo kinematics of the tibiotalar and subtalar joints in asymptomatic subjects: a high-speed dual fluoroscopy study. J. Biomech. Eng. 138.

Rosenbaum, D., Bertsch, C., Claes, L.E., 1997. NOVEL award 1996: 2nd prize Tenodeses do not fully restore ankle joint loading characteristics: a biomechanical in vitro investigation in the hind foot. Clin. Biomech. (Bristol, Avon) 12, 202–209.

Rosenbaum, D., Becker, H.P., Wilke, H.J., Claes, L.E., 1998. Tenodeses destroy the kinematic coupling of the ankle joint complex. A three-dimensional in vitro analysis of joint movement. J. Bone Joint Surg. (Br.) 80, 162–168.

Sanchez-Adams, J., Leddy, H.A., McNulty, A.L., O'Conor, C.J., Guilak, F., 2014. The mechanobiology of articular cartilage: bearing the burden of osteoarthritis. Curr. Rheumatol. Rep. 16, 451.

Schmid, B., 2010. Computational Tools for the Segmentation and Registration of Confocal Brain Images of *Drosophila melanogaster*. Universitat Wurzburg.

Scott, S.H., Winter, D.A., 1991. Talocrural and talocalcaneal joint kinematics and kinetics during the stance phase of walking. J. Biomech. 24, 743–752.

Sheehan, F.T., 2010. The instantaneous helical axis of the subtalar and talocrural joints: a non-invasive in vivo dynamic study. J. Foot Ankle Res. 3, 13.

Siegler, S., Chen, J., Schneck, C., 1988. The Three-Dimensional Kinematics and Flexibility Characteristics of the Human Ankle and Subtalar Joints—Part I: Kinematics.

Steinmetz, N.J., Aisenbrey, E.A., Westbrook, K.K., Qi, H.J., Bryant, S.J., 2015. Mechanical loading regulates human MSC differentiation in a multi-layer hydrogel for osteochondral tissue engineering. Acta Biomater. 21, 142–153.

Subburaj, K., Souza, R.B., Stehling, C., Wyman, B.T., Le Graverand-Gastineau, M.P., Link, T.M., Li, X., Majumdar, S., 2012. Association of MR relaxation and cartilage deformation in knee osteoarthritis. J. Orthop. Res. 30, 919–926.

Taga, I., Shino, K., Inoue, M., Nakata, K., Maeda, A., 1993. Articular cartilage lesions in ankles with lateral ligament injury. An arthroscopic study. Am. J. Sports Med. 21, 120–126 discussion 126-127.

Tavana, S., Clark, N., Newell, N., Calder, J.D., Hansen, U., 2020. In vivo deformation and strain measurements in human bone using digital volume correlation (DVC) and 3T clinical MRI. Materials 13.

Valderrabano, V., Hintermann, B., Horisberger, M., Fung, T.S., 2006. Ligamentous posttraumatic ankle osteoarthritis. Am. J. Sports Med. 34, 612–620.

van den Bogert, A.J., Smith, G.D., Nigg, B.M., 1994. In vivo determination of the anatomical axes of the ankle joint complex: an optimization approach. J. Biomech. 27, 1477–1488.

van Diepen, P.R., Dahmen, J., Altink, J.N., Stufkens, S.A.S., Kerkhoffs, G., 2020. Location distribution of 2,087 osteochondral lesions of the talus. Cartilage 13 (Suppl 1), 1344S–1353S.

Wainright, W.B., Spritzer, C.E., Lee, J.Y., Easley, M.E., DeOrio, J.K., Nunley, J.A., DeFrate, L.E., 2012. The effect of modified Broström-Gould repair for lateral ankle instability on in vivo tibiotalar kinematics. Am. J. Sports Med. 40, 2099–2104.

Wan, L., de Asla, R.J., Rubash, H.E., Li, G., 2006. Determination of in-vivo articular cartilage contact areas of human talocrural joint under weightbearing conditions. Osteoarthr. Cartil. 14, 1294–1301.

Wan, L., de Asla, R.J., Rubash, H.E., Li, G., 2008. In vivo cartilage contact deformation of human ankle joints under full body weight. J. Orthop. Res. 26, 1081–1089.

Westerweel, J., Scarano, F., 2005. Universal outlier detection for PIV data. Exp. Fluids 39, 1096–1100.